Investigations on a new slotless homopolar hybrid active magnetic bearing

Guillaume Colinet and Bruno Dehez

Institute of Mechanics, Materials and Civil Engineering (IMMC)
Université catholique de Louvain (UCLouvain)

Abstract

Homopolar hybrid active magnetic bearings generate very low power losses thanks to the absence of bias currents and the homopolar distribution of the magnetic flux density in the airgap. However, the slots in which the winding of these bearings are inserted create fluctuations of the magnetic flux density which are at the origin of iron losses that can be non-negligible at high speeds. This paper investigates a new slotless topology of homopolar hybrid active magnetic bearings, which can totally remove these losses. An electromagnetic model based on a magnetic circuit is proposed and validated through finite element simulations. It is then used to optimize and compare the performances of this original bearing topology with an existing slotted hybrid homopolar bearing.

1 Introduction

Active magnetic bearings (AMB) generate a contact-free guiding of a rotor by actively controlling the current flowing in an armature winding. Compared with other bearings, AMB have the advantages to create very low friction as well as to operate without lubrication and mechanical wear. They are therefore widely used in industrial applications, such as in turbomachinery, from smallturbo molecular pumps to large turbogenerators, in energy storing flywheels, in momentum flywheels or even in ventricular pumps [3] [4]. The vast majority of AMB used in industry relies on a heteropolar bias magnetic flux density created by a DC component of current, superimposed to the control currents, and have thus the drawback of generating Joule losses. This is the reason why hybrid active magnetic bearing (H-AMB) topologies using permanent magnets have been proposed to solve this problem [1] [5]. Among those H-AMB topologies, those having 8 poles are widely used [9] [8]. However, for those topologies, the bias magnetic flux density in the airgap alternate between a positive and a negative value and therefore generates iron losses in the rotor during its rotation. Alternative heteropolar topologies, that have less number of poles, have been proposed to reduce these losses [12]. Beyond heteropolar topologies, homopolar hybrid AMB (HH-AMB) produces less iron losses because the polarity of the bias magnetic flux density does not vary with the position of the rotor [11] [6]. However, there are still some fluctuations of the magnetic flux density due to the slots within which the armature winding is placed. To reduce further those fluctuations, slotless hybrid homopolar AMB (SHH-AMB) have been proposed [13] [7]. Those kind of magnetic bearings drastically reduce and even theoretically remove rotor core losses due to the bias magnetic flux density, which makes it attractive for applications in the vacuum or at very high-speed. However, in the proposed topologies, the PM are placed on the rotor in a surface-mounted configuration, which makes the mechanical design of those bearings more difficult. In this context, this paper explores a new slotless homopolar hybrid topology whose PM are placed in the stator, but more singularly, inserted between two ring-shaped iron poles. This feature fundamentally changes the way the magnetic flux density is redistributed in the airgap when the rotor is off-centered. The principle of force generation is therefore different which could open the way to a potential increase in the performances of the AMB.
This paper has the following structure. Section II gives a description and a parametrization of the proposed SHH-AMB. Section III provides an electromagnetic model of the AMB that allows to link the dimensional parameters of the SSH-AMB to performance criteria while section IV presents a comparison of this model with a FEM model. In section V, a parametric analysis is performed in order to study the influence of the parameters of the SHH-AMB over the two performance criteria. Finally, the results of a bi-objective optimization combining the two performance criteria as well as a comparison of these latter with an existing slotted HH-AMB proposed in [6], are presented in section VI.

2 Magnetic bearing description and parametrization

The AMB considered in this study is shown in Figure 1. The stator is made of a PM ring inserted between two ring-shaped iron poles and a concentrated winding located in the airgap between the stator iron poles and the rotor.
The PM is polarized in the axial direction and creates a bias magnetic flux that it is guided radially inward in the airgap on the right iron pole and radially outward in the airgap on the left iron pole, as highlighted with the white arrows in Figure 1. It is thus a homopolar topology, as the magnetic flux density produced in the airgap by the PM is supposed to be perfectly

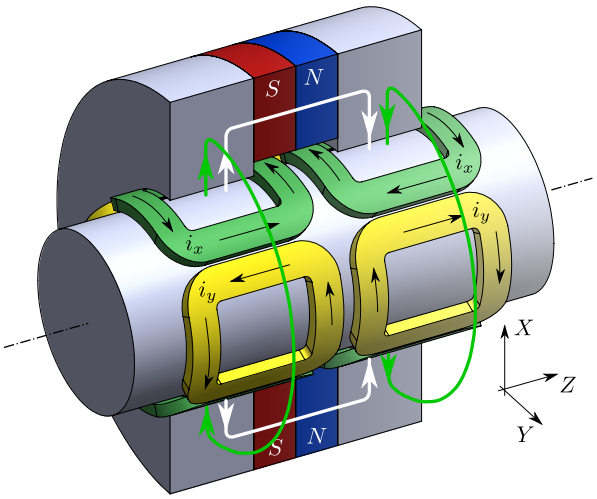

Figure 1: 3D view of the AMB.

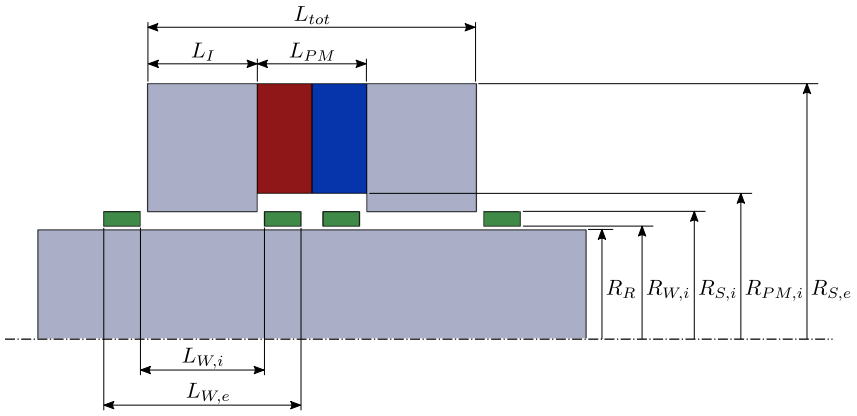

Figure 2: Parametrization of the AMB.

constant and independant of the angular position, when the rotor is centered radially.
The winding is made of four concentrated coils for each of the two radial axes. Two of them are placed at one iron pole with their magnetic axis pointing in the same direction as the axis under consideration, and the other two at the other iron pole but with their magnetic axis pointing in the opposite direction. The force generation relies in the unbalance of the magnetic pressure in the airgap arising from the superposition of the bias flux and the control flux created by the winding. Figure 1 highlights with the green arrows the control magnetic flux resulting in a force aligned with the positive X-axis. On the left iron pole, the control magnetic flux is directed such that it increases the magnetic pressure at the top and decreases it at the bottom, creating therefore an upward force on the rotor. On the right iron pole, the bias magnetic flux and the control magnetic flux are directed in the opposite direction, in order to also increase the magnetic pressure at the top and decrease it at the bottom.

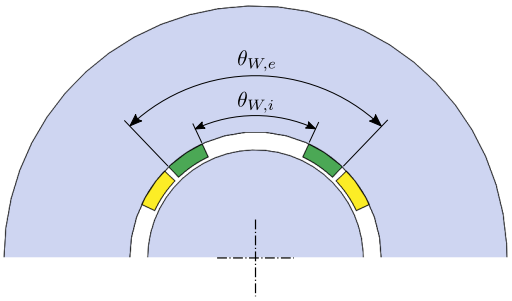

Figure 3: Parametrization of the AMB.

3 Modeling

The performances of an AMB are related to the force that is produced on the rotor. The resulting force that acts on the rotor has different components. The first component is the electrodynamic force, that arises from the interaction between the current i_x and i_y flowing respectively in the coils for the X-axis and the Y-axis and the magnetic flux of the PM that is linked by those coils. This force is related to the current through the the current stiffness k_i. By controlling the current in the winding, this force stabilizes the rotor in its centered position. The second component is the detent force, due to the interaction between the PM and the rotor iron. This force is related to the position x or y of the rotor with respect to the centered position through the position stiffness k_e. This force appears only when the rotor is off-centered, but it is directed in the same direction as the one of the off-centering, giving rise to instabilities. The third component is the reluctant force. It is due to the variation of the inductance of the winding with the rotor position and it is proportionnal to the square of the current.
In the centered position, because of symmetry, this reluctant force and its derivative relative to the rotor position is nul. For the same reason, the potential corss coupling between the two radial axes is non-existent. In consequence, in the centered position, the force acting on the rotor is given by:

$$\begin{cases} F_x = -k_e\, x + k_i\, i_x \\ F_y = -k_e\, y + k_i\, i_y \end{cases} \tag{1}$$

In this section, a model of the magnetic flux density due to the PM is first provided. From this latter, the current stiffness and the position stiffness are derived. Finally, as the force is linked to the current that flows in the winding, a model of the electrical resistance is also provided, to evaluate the Joule losses.

3.1 Airgap magnetic flux density

The magnetic flux density in the airgap, due to the PM, is obtained in two steps. The first consists in determining the magnetic potential difference between the stator and the rotor by solving the magnetic circuit shown in Figure 4. This latter assumes an infinite magnetic permeability of both the stator iron poles and of the rotor. The PM ring can be reprensented by its Northon representation with a flux source :

$$\phi_{PM} = B_r \cdot \pi(R_{S,e}^2 - R_{PM,i}^2) \tag{2}$$

in parallel with its internal permeance:

$$P_{PM} = \frac{L_{PM}}{\mu_0 \cdot (R_{S,e}^2 - R_{PM,i}^2)} \tag{3}$$

where B_r is the remanent flux density, $R_{S,e}$, $R_{PM,i}$ and L_{PM} are respectively the external radius of the stator, the internal radius of the PM and the length of the PM and μ_0 is the magnetic permeability of the vacuum.
The leakage magnetic flux going between the left and right outer radial surfaces of the stator iron parts, is taken into account by the permeance P_{PMfe}. According to [2], this permeance can be approximated using the following expression:

$$P_{PMfe} = 2\,\mu_0\,R_{S,e}\,ln\left(1 + \frac{2\,\pi \cdot R_{S,e}\,L_I + \pi\,L_I^2}{2\,L_{PM}\,R_{S,e}}\right) \tag{4}$$

where L_I is the axial length of one stator iron pole. The leakage magnetic flux going between the inner lateral surfaces of the stator iron poles. It is modeled by the permeance P_{PMfi}, whose expression is given by:

$$P_{PMfi} = \frac{\mu_0\,\pi\,(R_{PM,i}^2 - R_{S,i}^2)}{L_{PM}} \tag{5}$$

where $R_{S,i}$ is the internal radius of the stator. The flux going through the airgap is taken into account by the permeance P_g, that depends on the rotor off-centering x. Considering that the magnetic flux is purely radial, this permeance is derived from:

$$P_g = \int_0^{2\pi} dP_g \tag{6}$$

where dP_g is the permeance of a radial flux tube located at angle θ relative to the X-axis and having an infinitesimal angular opening $d\theta$. This latter is given by:

$$dP_g = \frac{\mu_0\,L_I}{\ln\left(\frac{R_{S,i} - x\cos\theta}{R_R}\right)}\,d\theta \tag{7}$$

where R_R is the external radius of the rotor. This function is not analytically integrable as it is, but considering that the off-centering x is small relative to the radii $R_{S,i}$ and R_R, on the one hand, and to the nominal airgap thickness $g = R_{S,i} - R_R$, on the other hand, it can be approximated first by developing the logarithm function in Taylor series limited to the first order so as to be rewritten:

$$dP_g = \frac{\mu_0\,L_I}{\ln\left(\frac{R_{S,i}}{R_R}\right) - \frac{x}{R_{S,i}}\cos\theta}\,d\theta \tag{8}$$

Next, as this function is a periodic function of θ, it can be expanded in Fourier series. Limited to the second order and its coefficients being themselves approximated but analytically, it results in:

$$dP_g = \frac{\mu_0 L_I}{\ln^3\left(\frac{R_{S,i}}{R_R}\right)}\left[\ln^2\left(\frac{R_{S,i}}{R_R}\right) - \left(\frac{x}{R_{S,i}}\right)\ln\left(\frac{R_{S,i}}{R_R}\right)\cos\theta + \left(\frac{x}{R_{S,i}}\right)^2\cos 2\theta\right]d\theta. \tag{9}$$

Using (6) and (9), the analytical expression of P_g finally reduces to:

$$P_g = \frac{2\,\pi\,\mu_0\,L_I}{\ln\left(\frac{R_{S,i}}{R_R}\right)}. \tag{10}$$

The fringing flux between the lateral surfaces of the stator iron parts and the rotor is taken into account by the permeances P_{gf}. According to [2], it can be expressed as follows:

$$P_{gf} = 4 \cdot \mu_0\,R_R\,ln\left(1 + \frac{y_{pgo2max}\,(2\,R_R + y_{pgo2max})}{y_{pgo2min}\,(2\,R_R + y_{pgo2min}}\right) \tag{11}$$

considering $y_{pgo2max} = R_{S,e} - R_{S,i}$ and $y_{pgo2min} = R_{S,i} - R_R$.

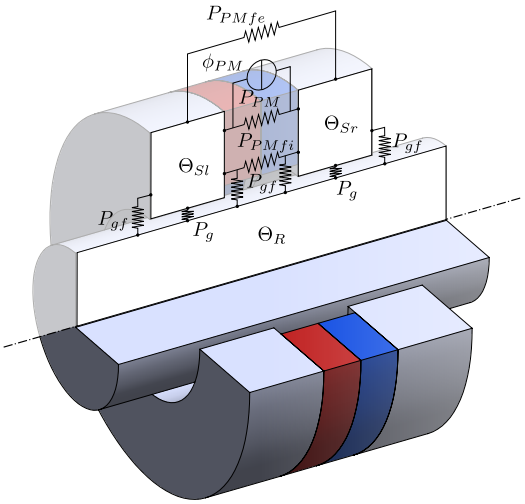

Figure 4: Magnetic circuit considering fringing effets.

Based on the equivalent circuit, the magnetic potential difference between the stator and the rotor $\Theta_{S-R} = \Theta_{Sl} - \Theta_R$ is directly given by:

$$\Theta_{S-R} = \frac{2\Phi_{PM}}{2\,P_{PMfe} + 2\,P_{PM} + 2\,P_{PMfi} + P_g + 2\,P_{gf}}. \tag{12}$$

The second step consists in determining the magnetic flux density in the airgap considering that the flux $d\Phi_g$ going through a radial flux tube having an infinitesimal angular opening $d\theta$ is given by:

$$d\Phi_g = \Theta_{S-R}\,dP_g. \tag{13}$$

As this flux is also the product of the normal section and the magnetic flux density, this latter is finally given by:

$$B_g = \frac{\mu_0\,\Theta_{S-R}}{r\ln^3\left(\frac{R_{S,i}}{R_R}\right)}\left[\ln^2\left(\frac{R_{S,i}}{R_R}\right) - \left(\frac{x}{R_R}\right)\ln\left(\frac{R_{S,i}}{R_R}\right)\cos\theta + \left(\frac{x}{R_R}\right)^2\cos 2\,\theta\right]. \tag{14}$$

3.2 Current stiffness

The electrodynamic force is related to the current through the current stiffness k_i. This latter can be expressed as the partial derivative relative to the off-centering x of the magnetic flux Ψ_x linked by the winding:

$$k_i = \frac{\delta \Psi_x}{\delta x}. \tag{15}$$

This flux can be obtained by summing the contributions of the fluxes $d\Psi_x$ linked by coils of infinitesimal section $dS_c = r\, dr\, d\theta$, whose $\frac{N_W}{S_W} dS_c$ go and back conductors are located respectively in (r, θ) and $(r, -\theta)$. Considering the four coils constituting the X-axis winding, the current stiffness is given by:

$$k_i = \frac{4\,\mu_0 L_I \Theta_{S-R}}{R_R \ln^2\left(\frac{R_{S,i}}{R_R}\right)} \frac{N_W}{S_W} \left(R_{S,i}^2 - R_{W,i}^2\right) \left(\cos\left(\theta_{W,e}/2\right) - \cos\left(\theta_{W,i}/2\right)\right) \tag{16}$$

where N_W and S_W are the number of turns and the section of one coil respectively.

3.3 Position stiffness

The position stiffness k_e is directly related to the detent force through:

$$k_e = \frac{\partial F_{detent}}{\partial x}. \tag{17}$$

This force can be derived by integrating the X-axis component of the magnetic pressure on the rotor surface facing the stator iron poles:

$$F_{detent} = 2\, L_I \int_0^{2\,\pi} \frac{B_g^2}{2\,\mu_0} \cos\theta\, R_R\, d\theta. \tag{18}$$

Using (14) and (18), (17) leads to:

$$k_e = 2\,\mu_0 \frac{\pi\, L_I\, \theta_{S-R}^2}{R_R^2 \ln^3\left(\frac{R_{S,i}}{R_R}\right)}. \tag{19}$$

3.4 Electrical resistance

The total resistance of one winding is given by:

$$R = 4\,\rho\, N_w \frac{L_{loop}}{S_c} \tag{20}$$

where ρ is the electrical resistivity, L_{loop}, the mean length of a loop, is given by:

$$L_{loop} = 2\, L_I + \left(\frac{R_{S,i} + R_{W,i}}{2}\right) \left[\frac{\pi}{2} \left(\theta_{W,e} - \theta_{W,i}\right) + 2\,\theta_{W,i}\right] \tag{21}$$

and S_c, the cross section of a conductor, is given by:

$$S_c = \eta \frac{S_W}{N_W} = \eta \frac{\left(\theta_{W,e} - \theta_{W,i}\right)\left(R_{S,i}^2 - R_{W,i}^2\right)}{4 N_W} \tag{22}$$

where η is the fill factor.

4 FEM validation

In order to validate the proposed model, its predictions are compared with those obtained from 3D FEM simulations. These latter have been performed with the software COMSOL Multiphysics ®. The parameters of the AMB used for this validation are given in Table 1. They corresponds to the parameters of the slotted HH-AMB proposed in [6], except for the parameters R_R, $R_{W,i}$, $\theta_{W,i}$ and $L_{W,e}$ that have been obtained by maximizing the bearing constant defined in (23).

Parameter	**Symbol**	**Value**	**Unit**
Total length of stator	L_{tot}	21	mm
Length of PM	L_{PM}	5	mm
Length of stator pole	L_I	8	mm
Internal length of winding	$L_{W,i}$	8	mm
External length of winding	$L_{W,e}$	12.748	mm
Radius of rotor	R_R	15.89	mm
Internal radius of winding	$R_{W,i}$	16.09	mm
Internal radius of stator	$R_{S,i}$	16.2	mm
Internal radius of PM	$R_{PM,i}$	33	mm
External radius of stator	$R_{S,e}$	35	mm
Internal angle of winding	$\theta_{W,i}$	1.2767	rad
External angle of winding	$\theta_{W,e}$	$\frac{\pi}{2}$	rad
Number of loops of a coil	N_W	95	/
Fill factor	η	0.4	/

Table 1: Parameters.

The evolution of the magnetic flux density in the airgap with the angular position, for a centered and off-decentered positions along the X-axis is shown in Figure 5. It can be seen that the analytical predictions overestimate the FEM ones by approximately 3%. This offset can be explained by the fact that the model does not consider the leakage flux between the PM ring and the rotor.

A comparison on the current stiffness shows that the analytical predictions underestimates the current stiffness by maximum 4%. Even if the magnetic flux density is overestimated by the analytical model, this underestimation can be explained by the fact the FEM model takes into account the flux linked the end-windings whereas the analytical model not.
A comparison on the position stiffness shows that the analytical model overestimates the FEM model by approximately 7%, independently of the off-centering amplitude. This difference can be explained by the higher magnetic flux density predicted by the analytical model.

The evaluation of this component of the force using the FEM model has shown that it represents less than 1% of the total force and therefore can be neglected.

5 Parametric analysis

In this section, the influence of the bearing parameters on its performances is studied. Those performances depend on the electrodynamic force, that should be as large as possible, and on the detent force, that should be as low as possible. Altough the latter can be evaluated using the position stiffness, the first one depends both on the current and on the current stiffness. For

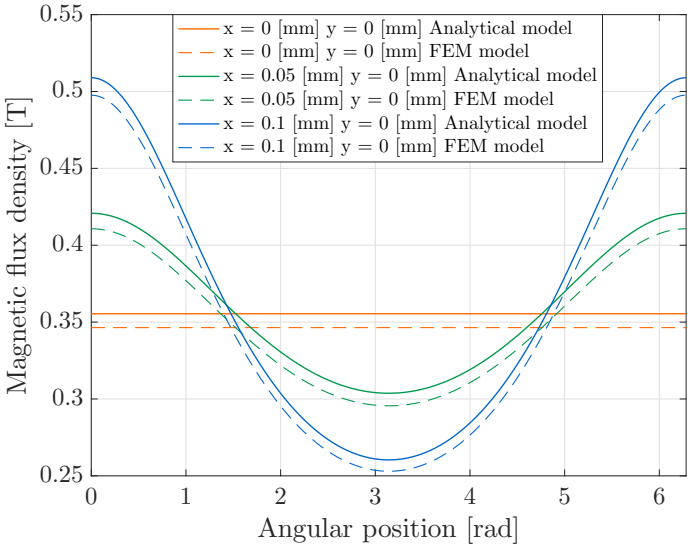

Figure 5: Magnetic flux density in the airgap.

the same current stiffness, an increase in the current would increase the electrodynamic force but this has to be limited because of the Joule losses and the temperature increase it generates. Therefore, an interesting criterion is the bearing constant defined as [10]:

$$k_b = \frac{k_i}{\sqrt{R}} \tag{23}$$

Indeed, mutliplying the numerator and the denominator by the current, the bearing constant reveals to be proportional to the ratio between the electrodynamic force and the square root of the Joule losses.
Based on these two performance criteria, a parametric analysis is performed. In a first step, the influence of the winding thickness and of the winding internal angle is studied, considering the parameters in Table 1. Then, keeping the best values for those two parameters, the influence of the other parameters is studied.

5.1 Winding thickness

The variation of the current stiffness, the electrical resistance, the bearing constant and the position stiffness with the winding thickness is shown in Figure 6. The current stiffness decreases when the thickness increases because it directly impacts the gap between the stator and rotor, and therefore reduces the airgap magnetic flux density. The number of loops beeing constant, the flux linked by the winding, as well as the resulting current stiffness have to follow the same evolution. Regarding the electrical resistance, it decreases with the winding thickness because, for a constant number of loops, the wire cross section increases with the winding section.

It can be seen that this effect has a much bigger impact for very small values of the thickness. Concerning the bearing constant, it reaches a maximum as the decrease in resistance predominates over the decrease in current stiffness for small thicknesses, whereas it is the opposite

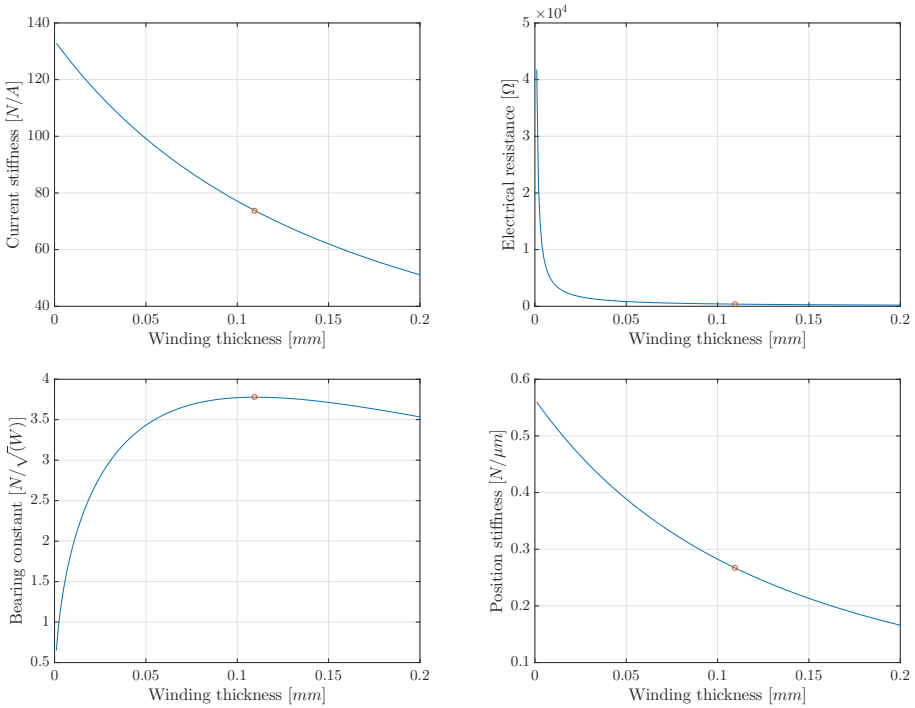

Figure 6: Analysis on winding thickness, ∘ corresponds to parameters in Table 1.

for larger thicknesses. The evolution of the position stiffness with the winding thickness quite logically looks close to the evolution of the current stiffness.

5.2 Winding internal angle

As shown in Figure 7, the current stiffness increases with the winding internal angle because each winding loop links a higher magnetic flux. Concerning the resistance, it increases slightly for small value and then increases fastly when this angle becomes close to the external angle of the winding. As shown by the evolution of the bearing constant, the increase of the resistance has more impact than the increase of the current stiffness and therefore the bearing constant is decreasing monotonically. The position stiffness is not influenced by the winding internal angle as this latter parameter does not modify the value of the magnetic flux density in the airgap.

5.3 Stator internal radius

As presented in Figure 8, a higher radius leads to a higher current stiffness. It can be explained by the fact that the winding covers a higher area and therefore links a higher magnetic flux, the airgap magnetic flux density remaining almost the same because the gap between the stator and the rotor is fixed. Concerning the resistance, it decreases with the value of the radius because the section of the winding increases. The effect on the current stiffness and the resistance goes in a way to increase the bearing constant. The radius has only a small impact on the position stiffness.

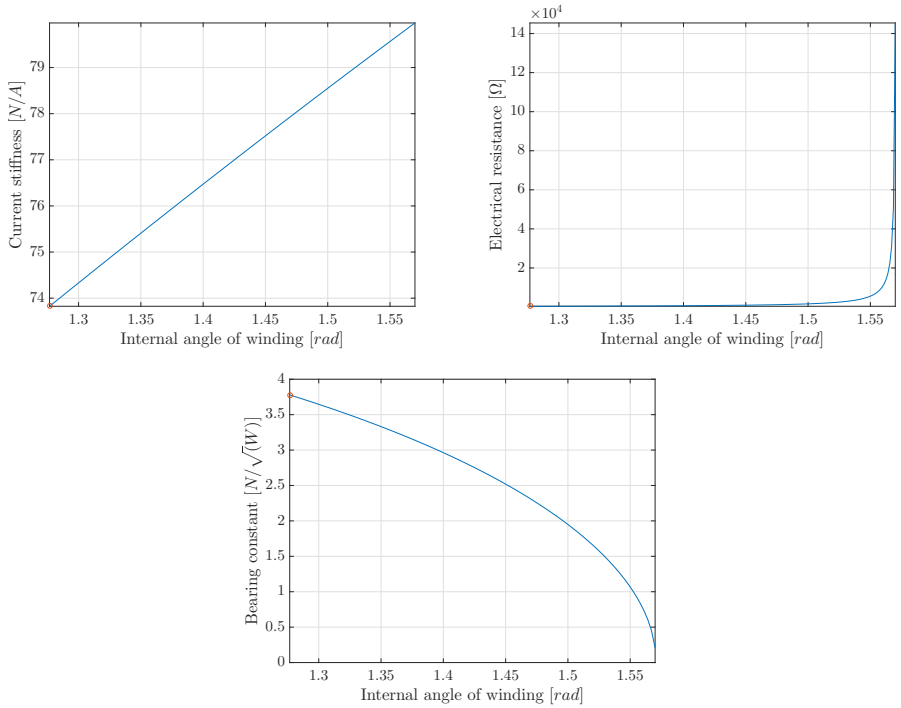

Figure 7: Analysis on winding internal angle, ∘ corresponds to parameters in Table 1.

5.4 Permanent magnet internal radius

The internal radius of the PM has a direct impact on the value of the magnetic flux density in the airgap. It can be seen in Figure 9 that the bearing constant, which has exactly the same shape as the current stiffness because the resistance does not vary, and the position stiffness depend almost linearly on the radius. However an increase of a given factor over the current stiffness is counterbalanced by an increase of the square of this factor in the position stiffness. Obviously, the electrical resistance is not affected by the PM internal radius.

5.5 Permanent magnet length

As the total length of the bearing $L_{tot} = 2L_I + L_{PM}$ remains constant in the analysis, the length of the PM is studied through the following parameter:

$$\alpha = \frac{L_{PM}}{L_{tot}} \tag{24}$$

As illustrated in Figure 10, the current stiffness reaches an optimum that can be explained by the respective evolutions with the magnet length of both the magnetic flux density in the airgap and the coil area. For increasing α, the airgap magnetic flux density increases as the leakage fluxes between the two stator ferromagnetic parts decrease on the one hand, while the coil area decreases on the other hand. For small values of α the airgap magnetic flux density increases faster than the surface of winding decreases, resulting in an increase of the current stiffness, while it is the opposite for high value of α.

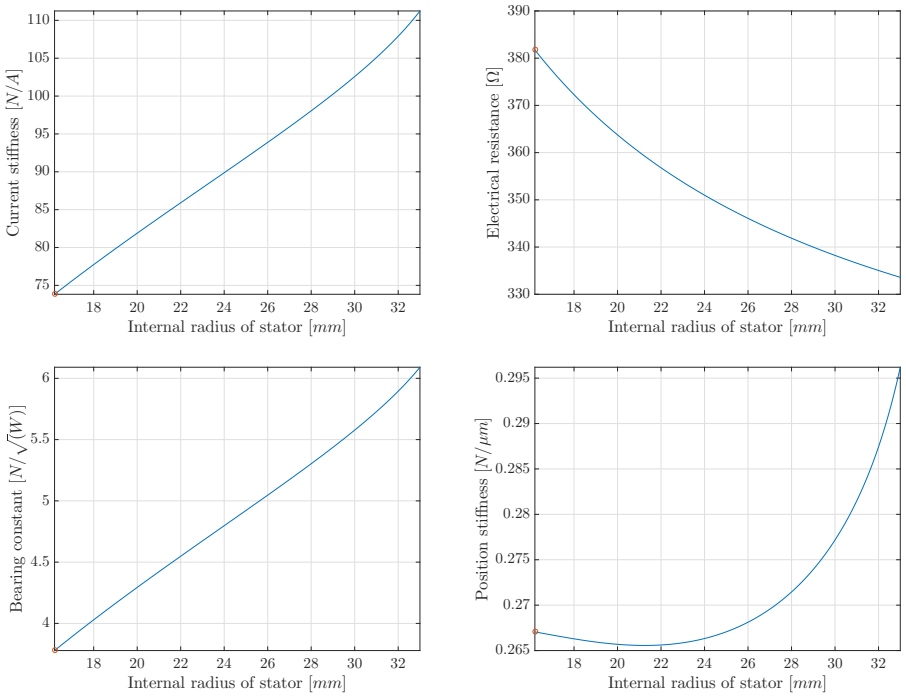

Figure 8: Analysis on stator internal radius, ∘ corresponds to parameters in Table 1.

The resistance decreases with α as it depends linearly on the stator pole length L_I. The position stiffness reaches a maximum but for higher α because of the square dependency of this stiffness on the magnetic flux density.

6 Optimization and comparison

A bi-objective optimization, considering the bearing constant k_b and the position stiffness k_e as two independant objectives is performed. The optimization parameters are R_R, $R_{S,i}$, $R_{PM,i}$ $\theta_{W,i}$, $\theta_{W,e}$ and α. The other parameters, more specifically $R_{S,e}$ and L_{tot}, are fixed to the ones in Table 1, . The optimization is performed using a sequential quadratic programming (SQP) algorithm. The results of the optimization process is shown in Figure 11 and consists of several optimizations applied on a single objective function combining with variable weights the two objectives. The Pareto front consists of the best compromise and is found between the extremas $(k_b, k_e) = (0, 0)$ and $(k_b, k_e) = (28.9, 40.5)$. In Figure 11, the geometry of two bearings from the Pareto front are shown. It can be seen that the bearing ∘ has a lower position stiffness due to the higher winding thickness and higher internal radius of PM. On the contrary, the bearing ⋄ reach a higher bearing constant because of the very low winding thickness and the lower internal radius of PM.
Comparing these results with those of the slotted homopolar AMB presented in [6] for which $(k_b, k_e) = (51.23, 0.57)$, shows that it is apparently not possible to reach the same value of the bearing constant. Furthermore, for the same position stiffness, the bearing constant is approximately five times lower.

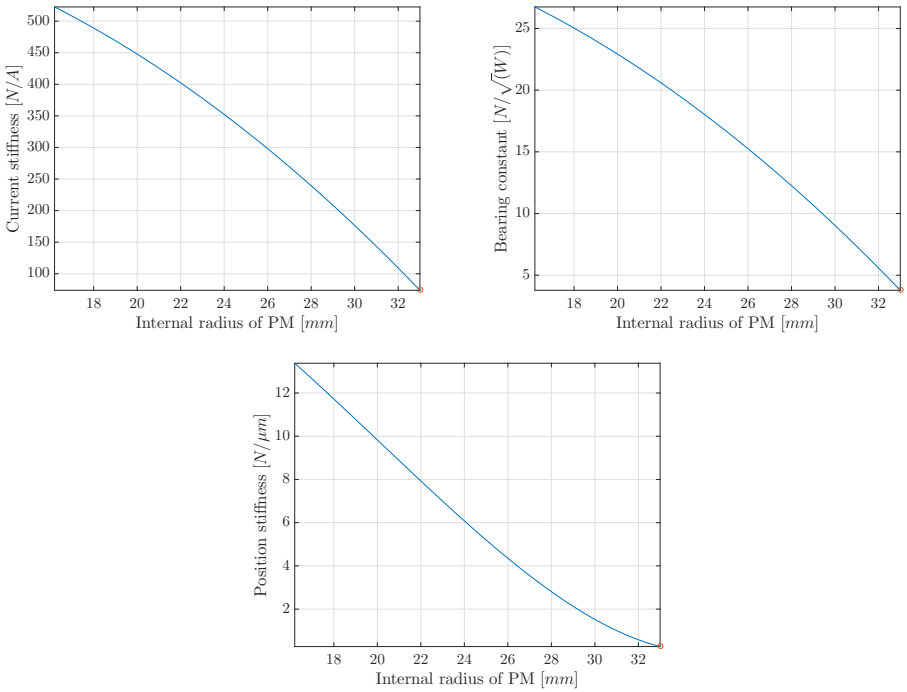

Figure 9: Analysis on PM internal radius, ∘ corresponds to parameters in Table 1.

7 Conclusion

In this paper, a new slotless HH-AMB that theoretically removes iron losses due to the bias magnetic flux density has has been studied. To that end an electromagnetic model that assumes small off-centering amplitude has been presented and validated by a FEM model. From that model, two performance criteria have been derived, the bearing constant, which reflects the force capability of the bearing through the current stiffness and the winding electrical resistance, and the position stiffness. On that basis, a parametric analysis has been carried out to understand the influence of the different dimensional parameters of the proposed bearing on its performances. Then, a Pareto front was obtained via an optimisation process. This revealed that the proposed bearing seems not able to reach the performances of slotted HH-AMB in terms of bearing constant. . However, these results have been obtained by imposing the same total length of the stator and the same external radius of the PM. Keeping the same volume of the AMB while varying those two parameters might give better results. In addition, these two HH-AMB should also be compared considering the iron losses, since the slotless topology should be better on this aspect.

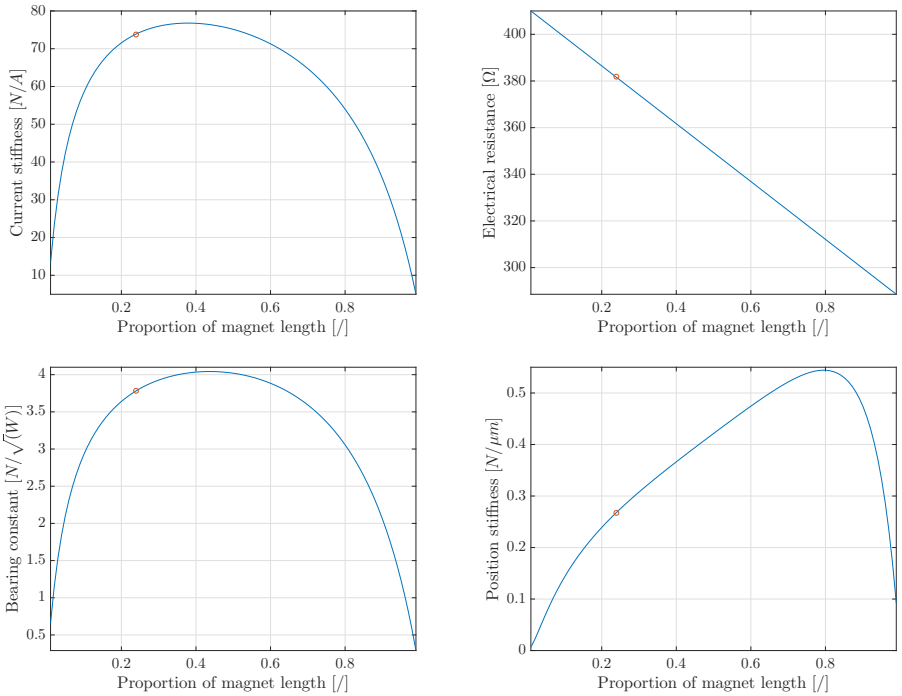

Figure 10: Analysis on PM length, ∘ corresponds to parameters in Table 1.

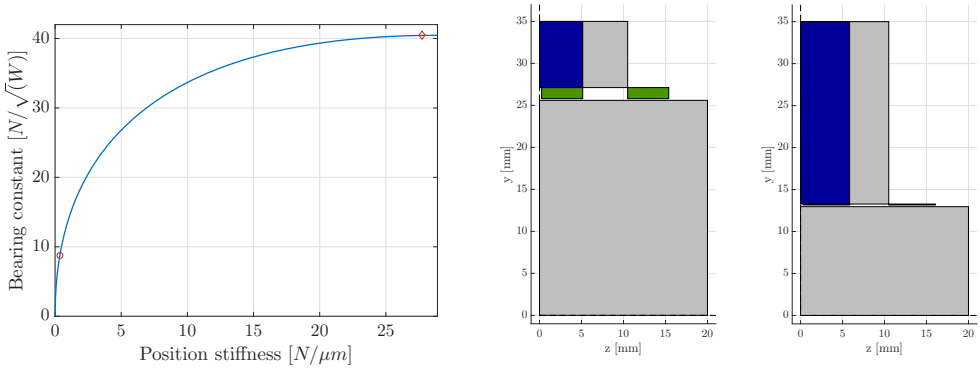

Pareto Front a: Bearing ∘ b: Bearing ⋄

Figure 11: Pareto front and geometry of 2 bearings.

References

[1] E. H. Allaire A. Studer and C. K. Sortore. Low power magnetic bearing design for high speed rotating machinery. *Int. Symposium on Magnetic Suspension Technology , Hampton, VA, USA, 1991*, 1991.

[2] M. A. Batdorff and J. H. Lumkes. High-fidelity magnetic equivalent circuit model for an axisym-

metric electromagnetic actuator. *IEEE Transactions on Magnetics*, 45(8):3064–3072, 2009.

[3] Alfons Traxler Gerhard Schweitzer, Hannes Bleuler. Active magnetic bearing foundation, performance and application. Yu Lie, Yuan Suijun, translation. Beijing: New Times Press. 1997.

[4] Eric H.Maslen Gerhard Schweitzer. Magnetic bearings:theory, design, and application to rotating machinery. Xu Yang, Zhang Kai, Zhao Lei translation. Beijing: Mechanical Industry Press,2012.

[5] L. Ji, L. Xu, and C. Jin. Research on a low power consumption six-pole heteropolar hybrid magnetic bearing. *IEEE Transactions on Magnetics*, 49(8):4918–4926, 2013.

[6] F. Jiancheng, W. Xi, W. Tong, T. Enqiong, and F. Yahong. Homopolar 2-pole radial permanent-magnet biased magnetic bearing with low rotating loss. *IEEE Transactions on Magnetics*, 48(8):2293–2303, 2012.

[7] Maurus Kaufmann, Arda Tüysüz, Johann W. Kolar, and Christof Zwyssig. High-speed magnetically levitated reaction wheels for small satellites. In *2016 International Symposium on Power Electronics, Electrical Drives, Automation and Motion (SPEEDAM)*, pages 28–33, 2016.

[8] Kenny and A. B. Palazzolo. Single plane rad ial, magnetic bearings biased with poles containing permanent magnets. *J. Mech. Des.*, 125:178–185, Mar. 2003.

[9] H. Koyanagi Okada and K. Kakihara. Miracb earing: New concept of miracle magnetic bearings. *Int. Symp. on Magnetic Bearings , Lexington, Kentucky, USA*, Aug. 2004.

[10] Patricio Peralta, Guzmán Borque-Gallego, Yoann Lapijover, and Yves Perriard. Experimental electromechanical characterization of slotted and slotless miniature bearingless drives. In *2021 IEEE International Electric Machines Drives Conference (IEMDC)*, pages 1–8, 2021.

[11] M. A. Pichot and M. D. Driga. Loss reduction strategies in design of magnetic bearing actuators for vehicle applications. *IEEE Transactions on Magnetics*, 41(1):492–496, 2005.

[12] R. Zhu, W. Xu, C. Ye, and J. Zhu. Novel heteropolar radial hybrid magnetic bearing with low rotor core loss. *IEEE Transactions on Magnetics*, 53(11):1–5, 2017.

[13] Christof Zwyssig, Thomas Baumgartner, and Johann W. Kolar. High-speed magnetically levitated reaction wheel demonstrator. In *2014 International Power Electronics Conference (IPEC-Hiroshima 2014 - ECCE ASIA)*, pages 1707–1714, 2014.